Water-in-Polymer Salt Electrolyte for Long-Life Rechargeable Aqueous Zinc-Lignin Battery

RESEARCH ARTICLE

Zinc Batteries

Energy & Environmental Materials WILEY

Water-in-Polymer Salt Electrolyte for Long-Life Rechargeable Aqueous Zinc-Lignin Battery

Divyaratan Kumar, Leandro R. Franco, Nicole Abdou, Rui Shu, Anna Martinelli, C. Moyses Araujo, Johannes Gladisch, Viktor Gueskine, Reverant Crispin, and Ziyauddin Khan**

Zinc metal batteries (ZnBs) are poised as the next-generation energy storage solution, complementing lithium-ion batteries, thanks to their cost-effectiveness and safety advantages. These benefits originate from the abundance of zinc and its compatibility with non-flammable aqueous electrolytes. However, the inherent instability of zinc in aqueous environments, manifested through hydrogen evolution reactions (HER) and dendritic growth, has hindered commercialization due to poor cycling stability. Enter potassium polyacrylate (PAAK)-based water-in-polymer salt electrolyte (WiPSE), a novel variant of water-in-salt electrolytes (WiSE), designed to mitigate side reactions associated with water redox processes, thereby enhancing the cyclic stability of ZnBs. In this study, WiPSE was employed in ZnBs featuring lignin and carbon composites as cathode materials. Our research highlights the crucial function of acrylate groups from WiPSE in stabilizing the ionic flux on the surface of the Zn electrode. This stabilization promotes the parallel deposition of Zn along the (002) plane, resulting in a significant reduction in dendritic growth. Notably, our sustainable Zn-lignin battery showcases remarkable cyclic stability, retaining 80% of its initial capacity after 8000 cycles at a high current rate (1 A g^{-1}) and maintaining over 75% capacity retention up to 2000 cycles at a low current rate (0.2 A g^{-1}). This study showcases the practical application of WiPSE for the development of low-cost, dendrite-free, and scalable ZnBs.

1. Introduction

The United Nations has identified 17 goals for the 2030 Agenda for Sustainable Development. Among these, goal 7 aims to ensure access to affordable, reliable, sustainable, and modern energy for all human beings.[1] Energy is a cornerstone for both developed and low-income countries that can lead to a positive impact on the society, economy, and environment.[2] Among all myriad energy technologies, energy storage acting as a buffer of energy has been identified as the bottleneck to further mass implement the renewable energy sources. Rechargeable batteries are considered in the strategies to provide stored energy for short time scale at demand.[3] Lithium-ion batteries (LiBs) are today not only mass implemented in portable electronics and electric vehicles, but also considered for buildings as a backup energy solution because of their versatile properties: high output voltage, high energy-to-weight ratio, charge and discharge at high currents, and low self-discharge.[4] Drawbacks are related to the safety issues due to thermal runaway and flammable liquid electrolytes as well as the fact that lithium and atomic elements such as cobalt used in electrodes have limited natural abundance. Finally, the carbon footprint of making LIBs is high as there is an emission of 75 kg CO_2 in making of 1 kWh LiBs.[5] These aspects have led researchers to explore the potential of rechargeable batteries based on alternative monovalent (Na, K) or multivalent (Mg, Ca, Zn, Al) elements of high abundance and low cost as next-generation battery technology beyond LiB technology.

Among multivalent ion batteries, rechargeable ZnBs normally called Zn ion batteries have captivated attention owing to the abundance of Zn, low cost, and low toxicity. Importantly, its redox potential is −0.76 V versus the standard hydrogen electrode (SHE), which makes ZnBs operable in non-flammable aqueous electrolytes.[6] Moreover, the high theoretical specific capacity (820 mAh g^{-1}), large volumetric capacity (5846 mAh mL^{-1}), >99% recyclability of Zn metal from used batteries, and low CO_2 emission (45.1 kg) for 1 kWh charge storage capacity makes the ZnB a frontrunner among the sustainable battery technologies that could compete with LiBs in some applications.[7] For instance, these properties enable large-scale manufacturing of ZnBs

D. Kumar, Dr. R. Shu, Dr. J. Gladisch, Dr. V. Gueskine, Prof. R. Crispin, Dr. Z. Khan
Laboratory of Organic Electronics, Department of Science and Technology, Linköping University, SE-60174, Norrköping, Sweden
E-mail: reverant.crispin@liu.se
E-mail: ziyauddin.khan@liu.se
D. Kumar, Dr. V. Gueskine, Prof. R. Crispin, Dr. Z. Khan
Wallenberg Wood Science Center, Department of Science and Technology (ITN), Linköping University, SE-60174, Norrköping, Sweden
Dr. L. R. Franco, Dr. C. Moyses Araujo
Department of Engineering and Physics, Karlstad University, 65188, Karlstad, Sweden
Dr. N. Abdou, Prof. A. Martinelli
Department of Chemistry and Chemical Engineering, Chalmers University of Technology, SE-41296, Gothenburg, Sweden
Dr. C. Moyses Araujo
Department of Physics and Astronomy, Uppsala University, 75120, Uppsala, Sweden
The ORCID identification number(s) for the author(s) of this article can be found under https://doi.org/10.1002/eem2.12752.

DOI: 10.1002/eem2.12752

which has been regarded as a safe, recyclable, cost-effective energy storage technology that can fulfill the sustainability goals set by the United Nations. However, there are also concerns associated with ZnBs which require immediate attention. One of the major concerns is the thermodynamic instability of unpolarized Zn metal in an aqueous electrolyte, whether acidic or basic. The negatively polarized Zn metal electrode in contact with aqueous electrolyte triggers the HER ($2H^+ \rightarrow H_2$), which raises the local pH around the electrode. As a result, a passivation layer of $Zn(OH)_2$ is formed on top of Zn.[8] The interplay between dendritic growth and HER leads to a degradation in the performance of ZnBs, such as cyclic stability and coulombic efficiency (CE) of Zn plating/-stripping. To suppress HER and dendritic growth in ZnBs, mainly two strategies have been employed: firstly, the surface modification of Zn anode with Zn alloys, or a coating of an inorganic or organic material,[9] and, secondly, the modification of the electrolyte by using additives or highly concentrated electrolytes.[10] Recently, one of the mechanisms proposed to suppress dendritic growth is the promotion of the Zn growth along its (002) plane.[11] Indeed, there seems to be a correlation between the (002) facets in a hexagonal close-packed Zn crystal that has the least surface energy and prevention of dendrite growth.[11]

In recent years, the strategy of super-concentrated electrolyte, also called WiSEs, was proposed to suppress HER by extending the electrochemical stability windows of aqueous electrolytes beyond 1.2 V.[12] This approach has also enabled the demonstration of aqueous electrolytes for LiBs,[13] Na-ion batteries,[14] and ZnBs.[15] Additionally, super-concentrated electrolytes also promote the reversibility of the electrochemical plating/stripping for Zn electrode. For example, Wang et al. demonstrated ~100% coulombic efficiency (CE) for Zn electroplating/stripping using 1 m $Zn(TFSI)_2$ + 20 m LiTFSI as WISE.[16] However, most of the ZnBs demonstrated using WiSE use high concentration of fluorinated salts such as those based on $(TFSI)^-$ or $(OTf)^-$, which are not only expensive but also have a negative environmental impact. Also, for ZnBs to reach commercial application, it is essential to develop WiSE with low or no fluorinated salts. Previously, our group provided the first indication of a new strategy to decrease the fluorinated salt in the electrolyte which can transport cations.[17] Indeed, low concentration (0.2 m) $Zn(TFSI)_2$ added to PAAK as a WiPSE could be utilized for Zn deposition.[17] This means that the WiPSE's ability to increase the stability windows does not come from the $Zn(TFSI)_2$ salt but from the non-fluorinated PAAK salt, while only a small amount of $Zn(TFSI)_2$ is added for the charge storage.[17] It is worth underlining that in our first study, Zn plating/stripping was not investigated systematically and no Zn-lignin battery was fabricated. This previous study investigated the electroactivity of lignin with various salts, including Li, Ca, Mg, and Zn in half-cell configuration; however, $Zn(TFSI)_2$-added PAAK was selected strategically to fabricate Zn-lignin battery as Zn can be electroplated contrary to other salts (Li, Ca and Mg) using PAAK.

In this work, we prepared PAAK + x m $Zn(TFSI)_2$ (x = 0.1 and 0.2) as WiPSE and systematically studied the Zn plating/stripping phenomena. The best performing electrolyte was found to be PAAK +0.2 m $Zn(TFSI)_2$ and has been integrated into a Zn-organic battery. This new strategy provides a stable Zn battery with significantly reduced electrolyte cost and a noteworthy cut in environmental impact by usage of low concentration of fluorinated salt. Moreover, it was observed that WiPSE facilitates Zn deposition via (002) plane which enables dendrite-free ZnB. The organic electrode chosen is the biopolymer lignin, which can be electrochemically active when combined with conductive carbon as demonstrated previously by Ail et al.[18] The resulting Zn-lignin battery in PAAK +0.2 m $Zn(TFSI)_2$ displayed 75 mAh g^{-1} of specific capacity, 80% retention in specific capacity, and >99% CE up to 8000 cycles.

2. Results and Discussion

2.1. Electrolyte Characterization

2.1.1. Electrochemical Stability Window, Ionic Conductivity, and Viscosity of WiPSE

In a precedent work, PAAK as WiPSE was synthesized and its transport properties were extensively characterized by our research group.[19,20] In this study, we prepared 0.1 and 0.2 m Zn^{2+}-added PAAK as a WiPSE for ZnBs with the objective of reducing the concentration of fluorinated salt without compromising the advantages of WiSE. After the preparation of the electrolyte, the electrochemical stability window (ESW) was determined, a key parameter for assessing the electrochemical stability of an electrolyte. On cathodic regions, Zn deposition and hydrogen evolution reaction (HER) were observed beyond −1.0 V versus Ag/AgCl, whereas on the anodic side, it was observed that the oxygen evolution reaction (OER) decreased significantly in PAAK-added $Zn(TFSI)_2$ electrolytes (Figure S1, Supporting Information).

The ionic conductivity of PAAK added with $Zn(TFSI)_2$, measured in a two-electrode cell by electrochemical impedance spectroscopy (EIS) (details can be found in experimental section), has been increased from 63.6 mS cm^{-1} (for PAAK only) to 91.6 mS cm^{-1} (for PAAK +0.05 m $Zn(TFSI)_2$) and then further it decreases to 73.8 mS cm^{-1} (for PAAK +0.2 m $Zn(TFSI)_2$) (Figure S2a, Supporting Information). The improved ionic conductivity of Zn-based electrolyte in comparison to PAAK could be attributed to the slightly reduced viscosity of the electrolyte [(Figure S2b, Supporting Information); detailed viscosity can be found in SI] and increased ionic concentrations.

2.1.2. Investigation of Zn^{2+} Solvation Structure by Molecular Dynamics Simulations

The introduction of different concentrations of $Zn(TFSI)_2$ to PAAK is expected to affect the solvation of ions as well as the dynamics of water and the polymer chains. **Figure 1** shows the Radial Distribution Functions (RDF) between selected atomic sites of the systems obtained by molecular dynamics simulations. Table S1, Supporting Information, gathers the specific distances of the RDFs and their respective coordination numbers. Zinc ions interact with the oxygen atoms of the polymer (Op), which is related to two phenomena: electrostatic interaction found in diluted solution, known as cation condensation along a polyanion, and the affinity of the oxygen electronic lone pairs to interact with metallic cations. In our case, Op belongs to the solvation shell of Zn^{2+} ions because polyanion behaves as a solvent to solvate the ions which was evidenced by short distance between Zn and Op (Figure 1c). The solvation shell begins at 1.64 Å, reaches a peak at 1.82 Å, and has a minimum at 2.79 Å (at 0.1 m $Zn(TFSI)_2$) or 2.63 Å (at 0.2 m $Zn(TFSI)_2$), comprising a number of 0.3 and 0.4 Zn ions at the concentrations of 0.1 and 0.2 m $Zn(TFSI)_2$, respectively. Such proximity of Zn^{2+} cations to the polymer chains leads to local dehydration of the polymer chains, resulting in the loss of approximately 0.6 water molecules per monomer at a concentration of 0.2 m $Zn(TFSI)_2$. The

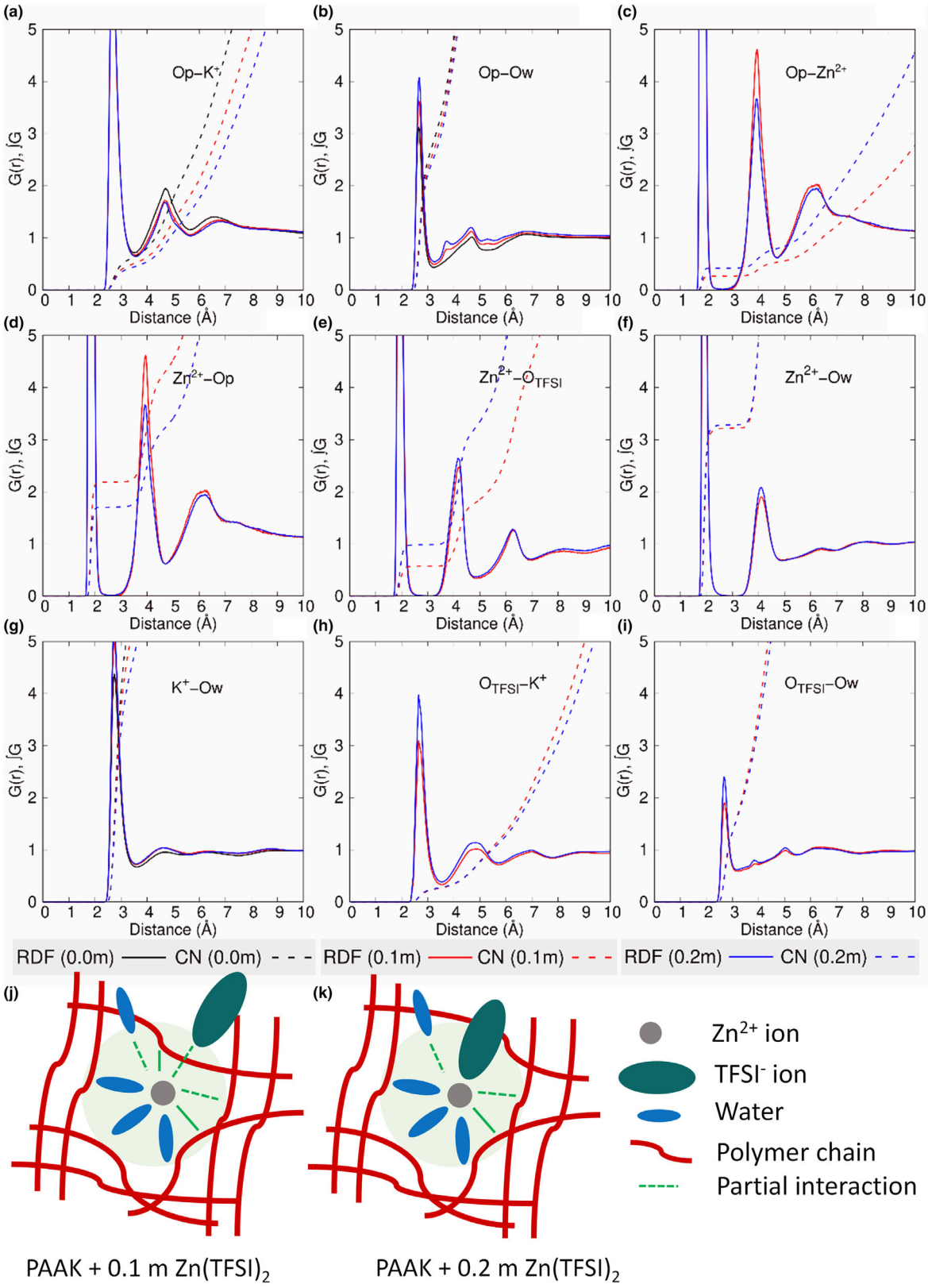

Figure 1. Radial distribution functions (RDF) and coordination numbers (CN) of the PAAK simulations at 0.0, 0.1 m and 0.2 m $Zn(TFSI)_2$ concentrations. a–c) Polymer oxygen (Op) interacting with potassium ion (K^+), water oxygen (Ow), and zinc ion (Zn^{2+}). d–f) Zn^{2+} interacting with Op, oxygen of $TFSI^-$ (O_{TFSI}^-) and Ow. g) K^+ interacting with Ow. h, i) O_{TFSI}^- interacting with K^+ and Ow. j, k) presents schematic illustration of solvation structure of hybrid electrolyte.

Table 1. Self-diffusion coefficients (D) computed for the species included in the MD simulations of PAAK-based electrolytes with $Zn(TFSI)_2$ concentrations equal to 0.0, 0.1, and 0.2 m.

Probed species	D (10^{-11} m^2 s^{-1})		
	0.0 m $Zn(TFSI)_2$	0.1 m $Zn(TFSI)_2$	0.2 m $Zn(TFSI)_2$
K^+	41.3 ± 0.1	23.2 ± 1.6	9.5 ± 1.7
Zn^{2+}	—	1.5 ± 0.4	0.5 ± 0.2
$TFSI^-$	—	6.9 ± 1.5	2.0 ± 0.7
PAA^-	2.3 ± 1.2	1.0 ± 0.3	0.3 ± 0.1
H_2O	93.9 ± 2.5	52.8 ± 2.7	26.4 ± 2.6

The self-diffusion coefficients were obtained from the slope of the MSD calculated from the MD simulations.

number of hydrogen bonds (N_{HB}) per monomer, formed between the polymer chain and water molecules, is 5.8 for a PAAK 1:2 solution without $Zn(TFSI)_2$, while it decreases to 4.6 at 0.1 m $Zn(TFSI)_2$ and 3.8 at 0.2 m $Zn(TFSI)_2$. This represents a reduction by 2 hydrogen bonds per monomer at the 0.2 m $Zn(TFSI)_2$ concentration. Figure S5, Supporting Information, shows the time evolution of key parameters characterizing the hydrogen bonds, that is, N_{HB}, donor-acceptor distance, and H-donor-acceptor angle distribution.

The local polymer chain dehydration by the addition of Zn salt is due to the interaction between Zn^{2+} ions and the negatively charged monomer. Now, we can observe the solvation shell around the Zn^{2+} cations. When Zn^{2+} ions are diluted in water, they can coordinate to six oxygen of water molecules[21] (Ow). In presence of PAAK and water, Zn^{2+} cations possess multiple oxygen types in their solvation shell either coming from acrylate or water. In a PAAK + x m $Zn(TFSI)_2$ (where $x = 0.1$, 0.2) electrolytes system, such oxygen coordination number keeps equal to 6 but these oxygen atoms come from different sources (Figure 1d–f). At a concentration of 0.2 m $Zn(TFSI)_2$, Zn^{2+} ions coordinate on average with 3.2 [3.3] oxygens of water molecules (Ow), 0.6 [1.0] oxygens of $TFSI^-$ ($O_{TFSI}{}^-$), and 2.2 [1.7] polymer oxygens (Op) (values in "[]" coordination number for 0.1 m $Zn(TFSI)_2$). In conclusion, Zn^{2+} ions preferentially interact with PAA^- rather than with $TFSI^-$. However, the interaction between Zn^{2+} and $TFSI^-$ increases with the $TFSI^-$ concentration. Moreover, it was observed that an average of 1 $O_{TFSI}{}^-$ in the first solvation shell of each Zn^{2+} ion indicates a tendency of Zn^{2+} and $TFSI^-$ to stabilize as a partially neutralized ion-pair in the PAAK electrolyte (Figure 1j,k).

The presence of $Zn(TFSI)_2$ salt also modifies the solvation of the K^+ ions, which suffer from a slight dehydration (see K^+ RDFs in Figure 1a,g). On average, the first solvation shell of K^+ in PAAK +0.2 m $Zn(TFSI)_2$ electrolyte has 1.4 less water molecules than in PAAK without the Zn salt. The number of K^+ ions coordinating to Op is slightly reduced by around 0.1 within the first solvation shell of Op because some K^+ ions interact instead with the $TFSI^-$ molecules (Figure 1h). Around 0.3 K^+ ions are found in the immediate vicinity of the $O_{TFSI}{}^-$ and $N_{TFSI}{}^-$. Finally, we analyzed the interaction between the oxygen and nitrogen atoms of $TFSI^-$ with water (Figure 1i). $O_{TFSI}{}^-$ exhibits a higher hydration level with a coordination number of 1.6 compared to $N_{TFSI}{}^-$ with a coordination number of 0.9.

Regarding the dynamics of the cations, anions and polymer chains, a significant and monotonic decrease in mass mobility is observed for all ions upon addition of $Zn(TFSI)_2$. In particular, K^+ ions and water molecules are most strongly slowed down. **Table 1** presents the self-diffusion coefficients (D) calculated from the slope of the atomic mean squared displacements (MSD). For comparison, D values were also computed for K^+ (201.9 ± 5.0), Zn^{2+} (76.5 ± 2.5), $TFSI^-$ (79.6 ± 5.9), and water (258.3 ± 0.9) in a water solution (at $T = 298$ K and $p = 1$ bar), expressed in units of 10^{-11} m^2 s^{-1}. In the presence of PAAK in the water and with 0.2 m of $Zn(TFSI)_2$, water diffusion and polymer diffusion exhibit values of 26.4 ± 2.6 and 0.3 ± 0.1 (10^{-11} m^2 s^{-1}), respectively, while K^+, Zn^{2+}, and $TFSI^-$ diffusion exhibit values of 9.5 ± 1.7, 0.5 ± 0.2, and 2.0 ± 0.7 (10^{-11} m^2 s^{-1}). Therefore, we observe that both Zn^{2+} ions and PAA^- polyanions exhibit similar diffusion rates, suggesting a robust mutual interaction between them. Compared to the dynamics of PAAK electrolyte, the introduction of $Zn(TFSI)_2$ leads to a reduction in the diffusion coefficient of all species but mostly for the PAA^-. Indeed, D decreases by a factor of 7.7 for this polymer, 4.3 for K^+, and 3.6 for water. As each Zn^{2+} ion attracts 3 water molecules from the solution, we can consider the existence of two very distinct micro-environments for water molecules; one primarily consisting of free water molecules, and another characterized by interactions with Zn^{2+} ions. In summary, our observations indicate a modification in the solvation structure of Zn^{2+}, with its solvation sheath now comprising PAA^-, $TFSI^-$, and water.

2.1.3. *Raman Spectroscopy of Zn(TFSI)$_2$-added PAAK*

The nature of the interactions between the different ionic species in both PAAK- and H_2O-based solutions was investigated by Raman spectroscopy. The interactions established between cations (Zn^{2+}, K^+) and anion ($TFSI^-$) are typically analyzed in the spectral range of the expansion-contraction mode of the $TFSI^-$ anion (ν_s S-N-S, ν_s CF_3 of the $TFSI^-$), which typically appears as an intense peak in the 741–744 cm^{-1} frequency range in the case of weakly coordinated TFSI-based complexes.[22–24] We therefore collected the Raman spectra of different PAAK- and H_2O-based solutions containing various amounts of the $Zn(TFSI)_2$ salt (see **Figure 2**a for Raman spectra of the PAAK-$Zn(TFSI)_2$ series). A thorough peak fitting analysis of the collected Raman spectra reveals that the position of the main component changes marginally keeping values close to 746.7 cm^{-1} upon adding $Zn(TFSI)_2$ to the PAAK electrolyte (Figure 2b). The trend shows a weak redshift of the frequency upon increased $Zn(TFSI)_2$ content, which is in qualitative agreement with the observed decreased viscosity (Figure S2b, Supporting Information). We also observe a systematic increase of this peak intensity with the concentration of $Zn(TFSI)_2$, which directly correlates to the increased amount of $TFSI^-$ anions in the detected sample volume (inset of Figure 2b).

For a better understanding of this finding, as well as for rationalizing the role of PAAK, Raman spectra were also recorded for neat (no PAAK) H_2O-based solutions with different $Zn(TFSI)_2$ salt concentrations (blue symbols in Figure 2b). We find that the Raman shift of the investigated vibrational mode increases slightly with composition but remains close to 746 cm^{-1}, keeping values just below those of the PAAK-based electrolytes (yellow symbols in Figure 2b). Based on the available literature on the correlation between Raman shift and inter-ionic interactions[16,25] the latter indicates that the $TFSI^-$ anion experiences, on average, stronger interactions in the PAAK-based electrolytes than in the neat H_2O-based electrolytes. This aspect corroborates with the result from MD simulations that $TFSI^-$ and Zn^{2+} are in closest proximity in the PAAK-based electrolyte (see e.g., Figure 1e); their interaction is possibly strengthened since water can screen less in the co-presence of K^+

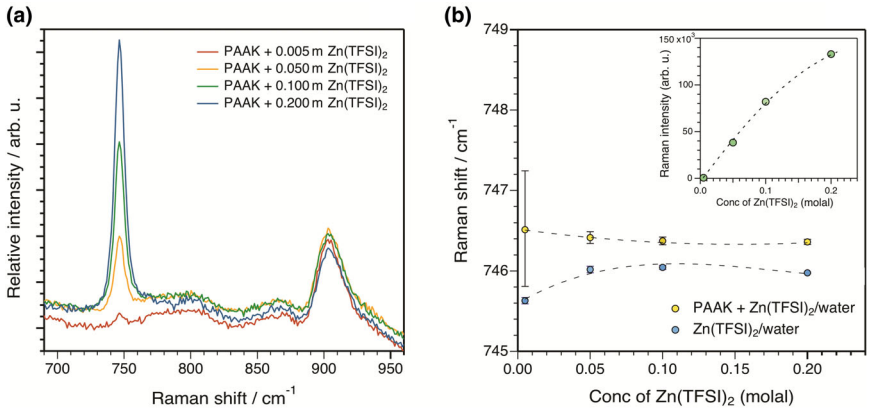

Figure 2. a) Raman spectra collected at room temperature for the PAAK-based electrolytes at different $Zn(TFSI)_2$ salt concentration; b) Raman shifts of the interaction sensitive mode (associated to the expansion/contraction of the $TFSI^-$ anion) as a function of the $Zn(TFSI)_2$ salt concentration, here found at ~746.6 cm^{-1}; the inset of b) shows Raman intensities calculated as the integrated area under the peak at ~746.6 cm^{-1}; dashed lines in b) are simple guides to the eye.

cations. Notably, the vibrational mode of $TFSI^-$ in the 4 m $Zn(TFSI)_2$ aqueous solution is observed at 747 cm^{-1} (Figure S10, Supporting Information), a blue shifted value that can be associated with the formation of strong Zn^{2+}-TFSI ion pairs, higher order complexes, or even $Zn(TFSI)_2$ crystals dispersed in the solute on, in agreement with this solution being at the limit of saturation. In summary, these results indicate that for intermediate concentrations (i.e., in the range 0.05–0.2 m of $Zn(TFSI)_2$ salt in solution), the interactions between $TFSI^-$ and its surrounding change slightly with composition (both in the PAAK- and the H_2O-based electrolytes) but are apparently stronger in the PAAK-based electrolytes.

Typically, polyanions are known to form a strong cross-linking network with multivalent cations such as Zn^{2+} ions.[26] However, despite the high concentration of PAAK, the added $Zn(TFSI)_2$ dissolved and formed a homogeneous clear solution without forming any precipitate (Figure S11, Supporting Information; digital image showing precipitation at lower concentration of PAAK). Furthermore, we observe that the viscosity of the prepared hybrid electrolyte decreases slightly with increasing the concentration of Zn^{2+} in PAAK (Figure S2b, Supporting Information), which disagrees with the hypothesis of the Zn^{2+} ions being strongly cross-linked with the PAA^- polyanions. In general, at low concentrations the electrostatic attraction between polyanions and cations is strong leading to the formation of a crosslinked network.[27] On the contrary, at high concentrations of the polymer, the electrostatic repulsion between the polyanionic chains becomes more pronounced and prevents the formation of crosslinked networks thereby decreasing the viscosity of the electrolyte. It would be worth mentioning here that previous studies on the interaction between PAA^- anions and Zn^{2+} showed that environment around the polyanion was largely independent on the concentration of Zn^{2+} ions.[28] Nonetheless, the MD simulations presented here reveal that the self-diffusion of PAA^- decreases by a factor of 8 with the addition of 0.2 m $Zn(TFSI)_2$ in PAAK, suggesting a strong polyanion interaction with Zn^{2+} cations. This information altogether indicates that even in the absence of precipitation a strong interaction exists between Zn^{2+} and PAA^-, both exhibiting slow diffusion rates. Given such peculiar properties, the question arises whether this type of WiPSE would enable reversible Zn plating, or not.

2.2. Zn Deposition and Morphological Properties

Zn plating/stripping in PAAK +0.1 m $Zn(TFSI)_2$ and PAAK +0.2 m $Zn(TFSI)_2$ electrolytes was investigated by cyclic voltammetry (CV) in a coin cell configuration using a Zn||Zn symmetric cell (**Figure 3a**). The voltammogram displays a pair of redox peaks originating from the reversible plating and stripping of Zn in both electrolytes which reveals that Zn can be plated and stripped using this hybrid WiPSE. In the CV, recorded at different sweep rates (Figure S12a, Supporting Information), the cathodic peak current (associated with $Zn^{2+} \rightarrow Zn$ process) displays a linear relationship with the square root of scan rate ($\nu^{1/2}$). This indicates that the electroplating process (nucleation, growth) is limited by a mass diffusion mechanism (Figure S12b, Supporting Information).[29,30] The long-term stability of Zn plating/stripping process in both these electrolytes was estimated under galvanostatic conditions at 0.1 mA cm^{-2} current rate by uninterrupted cycling. In both WiPSEs, the average voltage polarization was about 150 mV, which is higher than other reported literature (Figure 3b).[16,31] The rate performance of Zn||Zn cell was also investigated at different current rates ranging from 0.1 to 2 mA cm^{-2} where increase in overpotentials with increase in current was observed (Figure S13, Supporting Information). This high overpotential could be attributed to the high viscosity and low Zn^{2+} concentration in our WiPSE. It is worth mentioning here that 0.2 m $Zn(TFSI)_2$ is the maximum concentration soluble in PAAK. The early cell breakdown was observed after continuous cycling up to 350 h for the cell using PAAK +0.1 m $Zn(TFSI)_2$ electrolyte, whereas the cell with 0.2 m $Zn(TFSI)_2$ in PAAK can withstand up to 750 h with small increase in voltage polarization upon cycling. Therefore, PAAK +0.2 m $Zn(TFSI)_2$ has been selected for further studies even though PAAK +0.1 m $Zn(TFSI)_2$ displayed superior ionic conductivity and self-diffusion coefficients. After more than 750 cycles, a uniform, dense and dendrite free morphology was observed (Figure 3c) by SEM analysis of the cross section of Zn electrode. Further, the high magnification SEM images reveal formation of Zn flakes (Figure 3d).

To understand the growth mechanism of Zn, plating/stripping processes were performed at different cycles (10 and 100 cycles) using two different Zn||Zn cells, whereby deposited Zn was characterized by ex-situ methods. We fixed the electrolyte composition to PAAK +0.2 m $Zn(TFSI)_2$. At low magnification (2 μm scale), the Zn deposit appears dense (**Figure 4a,c**) whereas in the magnified images (200 nm scale) layered plate structures are visible (Figure 4d). The cell, which was cycled 100 times, displayed the formation of a hexagonal structure of Zn (see the inset marked in yellow dotted line in Figure 4c). Those hexagonal patterns are composed of several layers of hexagonal Zn (002) plane aligned above each other and parallel to the Zn metal surface. Importantly, there is no dendrite formation on those surfaces (Figure 4d). To examine the purity of deposited product, X-ray diffraction (XRD) was performed on both samples and compared it with pristine Zn. All the diffraction peaks were assigned to pure hexagonal Zn (JCPDS card 04-0831) with no impurity peaks in the diffractogram (Figure 4e). The XRD of Zn after 100 cycles displays an increase in the

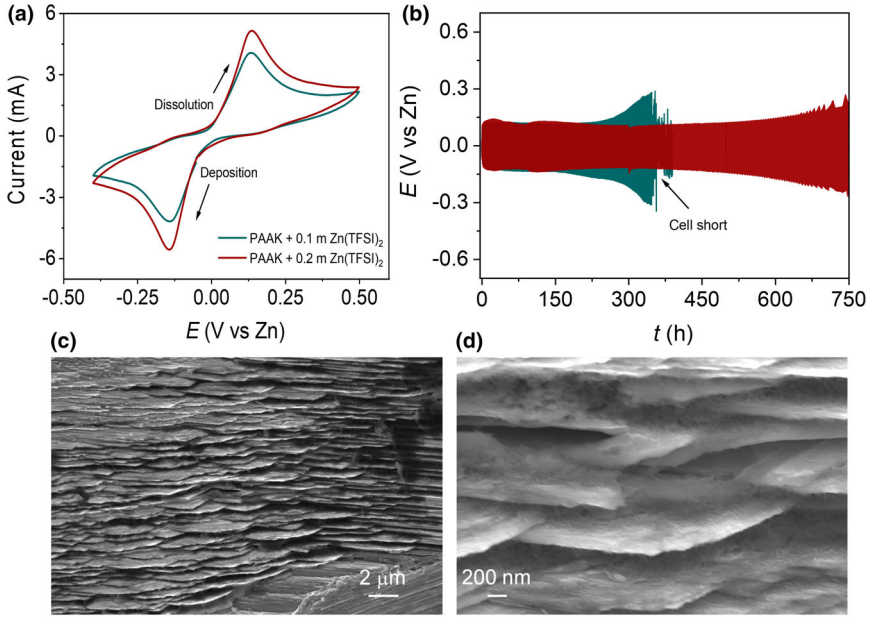

Figure 3. a) CV in PAAK +0.1 m $Zn(TFSI)_2$ and PAAK +0.2 m $Zn(TFSI)_2$ in the potential range of −0.4 to 0.5 V at 2 mV s^{-1}. b) Comparison of voltage profiles and cyclic stability of a Zn||Zn symmetric cell at 0.1 mA cm^{-2}, in a coin cell configuration in PAAK +0.1 m $Zn(TFSI)_2$ and PAAK +0.2 m $Zn(TFSI)_2$ (color coding is same as in 2a). Cross-sectional SEM images of Zn electrodes after 750 cycles in PAAK+ 0.2 m $Zn(TFSI)_2$ at c) 2 µm and d) 200 nm magnification scales.

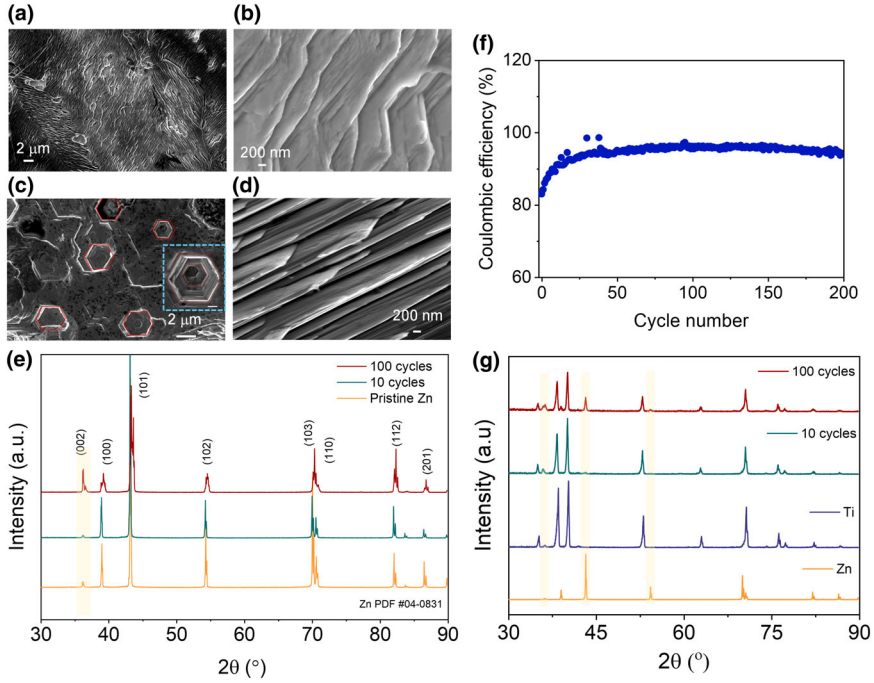

Figure 4. a) SEM images of Zn electrodes after a) and b) 10 cycles; c) top and d) cross-section after 100 cycles in PAAK+ 0.2 m $Zn(TFSI)_2$. The inset of c shows formation of hexagonal pattern Zn (scale bar is 200 nm). e) XRD of pristine Zn and Zn after 10 and 100 cycles of deposition/stripping using two different symmetric Zn||Zn cells showing deposition of pure Zn as no impurity peaks were observed. f) Coulombic efficiency related with Zn deposition on Ti in a Ti||Zn-based symmetric cell in PAAK+ 0.2 m $Zn(TFSI)_2$ to observe reversibility of Zn deposition. g) the XRD of Ti subjected to charge–discharge for 10 and 100 cycles at 0.1 mA cm^{-2} current rate. Zn deposition via (002) plane can be clearly seen on Ti surface without any impurity.

intensity of the (002) peak in comparison to the (100) peak as estimated by the ratio of $I_{(002)}/I_{(100)}$ for Zn plating, which increases with cycles. For bare Zn, the $I_{(002)}/I_{(100)}$ ratio is 0.49, increasing to 0.69 after 10 cycles, and further to 1.02 after 100 cycles. This implies that Zn^{2+} ions deposit along (002) plane. The growth of Zn deposit along (002) plane is advantageous for the formation of dendrite-free Zn structure compared to (101) plane.[32–34] Contrary to the (002) plane, the (101) plane is vertically aligned to the Zn surface, hence promoting dendritic growth. Also, the (002) crystal plane retains a high activation energy for Zn dissolution, thus suppressing the side reactions during cycling and hampering the growth of dendrites.[35]

The Zn plating/stripping reversibility was further investigated in PAAK +0.2 m $Zn(TFSI)_2$ using an asymmetric Ti||Zn as half-cell. The coulombic efficiency (CE) was calculated by ratio of Zn stripped from Ti to the Zn deposited during the same cycle. It can be deduced from the results that the CE gradually increases with cycles and reaches >95% up to 200 cycles (Figure 4f). Importantly, this result indicates that most of the deposited Zn on Ti substrate could be retrieved during the successive stripping processes. Ex-situ XRD was performed on the Ti used to deposit Zn at different cycles (10 and 100 cycles). The peak intensity of the (002) plane increased steadily after 10 cycles and continued to increase even more after 100 cycles (Figure 4g). This was also confirmed by estimate the peak intensity ratio of (002) plane to (101) plane which increases from 0.49 to 0.98 with cycling. This is reminiscent of a uniform and parallel deposition of Zn on the Ti surface. The other distinctive peaks in the diffractogram at 43.2° and 54.3° corroborate the pure Zn deposition (marked with light yellow strip).

Electrochemical quartz crystal microbalance (EQCM) is the technique we used to quantify the amount of deposited Zn from PAAK +0.2 m $Zn(TFSI)_2$. The quartz crystal is coated by a gold layer acting as the working electrode and its resonance frequency is followed versus the applied potential controlling the deposition/stripping. A CV comprising 15 cycles was carried out, with the potential swept between −0.3 and −1.6 V at a scan rate of 1 mV s^{-1}. During the first sweep, as the potential reached approximately −1.2 V, a substantial amount of Zn (~50 µg cm^{-2}) was deposited (Figure S15, Supporting Information) which increases further on the reversal of potential before reduction in mass starts. This kind of behavior is similar to the previously reported WiSE

systems.[36] In the potential range of −0.3 to −1.6 V, the initial Zn deposition was not completely stripped; however, in subsequent cycles, a mass increase and decrease were observed above the initial deposition level, indicating reversible exchange of Zn in the electrolyte and Au on the surface. As the number of cycles increased, the overall deposited mass also increased. In contrast to the observations in the electrolyte PAAK without $Zn(TFSI)_2$, a loss of mass was noticed, suggesting that Au from the quartz surface was leaving the surface.

2.3. Zn-Lignin Battery Characterization in PAAK +0.2 m $Zn(TFSI)_2$

In the Zn-lignin battery, the lignin electrode is a composite made of the insulating lignin and the conducting carbon nanoparticles with a 1:1 weight ratio. Those materials were mixed using ball milling method to obtain electronically conductive and electrochemically active lignin-carbon (L-C) nanocomposite. It is worth mentioning that ball milling helps to achieve an intimate interface between lignin and carbon.[18] The electrochemical analysis of Zn in the hybrid electrolyte was presented comprehensively in the previous section, while the half-cell study of L-C electrode was performed in one of our previous studies.[17] We now demonstrate a low-cost, sustainable Zn-lignin battery, where two abundant materials, Zn and L-C, are chosen as electrodes, by fabricating a 2032 type coin cell (**Figure 5**a). The specific capacity, specific energy, and self-discharge of the cell were thereby estimated. In Zn-lignin battery, lignin undergoes oxidation–reduction reaction, whereas Zn plates/strips at the Zn anode. Thus, the reversibility of Zn stripping/plating is coupled to the reversibility of redox reaction at the lignin electrode. The CV of Zn and L-C shows that the position of redox peak potentials of Zn and L-C lies in from −0.4 to 1.7 V versus Zn, thus L-C and Zn can be used as positive and negative electrode, respectively, in the assembled battery (Figure 5b). Based on the redox potential of those two electroactive materials a cell with 1.3 V potential can be achieved. The voltammogram at 5 mV s^{-1} of the Zn-lignin cell (Figure 5c) shows one broad oxidation and one broad reduction peak, where the former one is attributed to the oxidation of C═C–O^- to C–C═CO in the L-C (shown in inset of Figure 5b). The peak currents increase with scan rates (from 10 to 50 mV s^{-1}), which suggests that the ionic and electronic charge transport, along with the interfacial redox processes, are fast.

To understand the charge storage better and to assess whether it is diffusion controlled (which is usually ascribed to faradaic processes) or capacitive, the relationship between current and scan rate was evaluated ($i = a\nu^b$), where i and ν are defined as peak current and scan rate (1–5 mV s^{-1}), respectively (Figure S16a, Supporting Information). In this relation, a and b are the constants which can be estimated by the intercept and slope of log(i) *vs* log(ν) plot. If the estimated value of b is close to 0.5, then the charge storage process occurs *via* diffusion-controlled process, whereas if it reaches close to 1, then mechanism is dictated by non-faradaic process. Herein, the slope was found to be 0.84 (Figure S16b, Supporting Information) which indicates that energy storage process is dominated by diffusion-controlled process originating from the Faradic redox processes of Zn and lignin in hybrid electrolyte. Further, the diffusion and capacitive contribution to total capacity was estimated by CV using the following equation,

$$i = k_1\nu + k_2\nu^{0.5} \quad (1)$$

where k_1, k_2 are constants. $k_1\nu$ and $k_2\nu^{0.5}$ are the contribution from capacitive controlled process and the faradaic controlled processes, respectively. Figure S16c, Supporting Information, illustrates the typical separations of capacitive and diffusive currents using Equation (1). We estimate that 85% of the total stored charge in the Zn-lignin cell is due to a faradaic process, whereas the remaining 15% is due the surface controlled capacitive process.

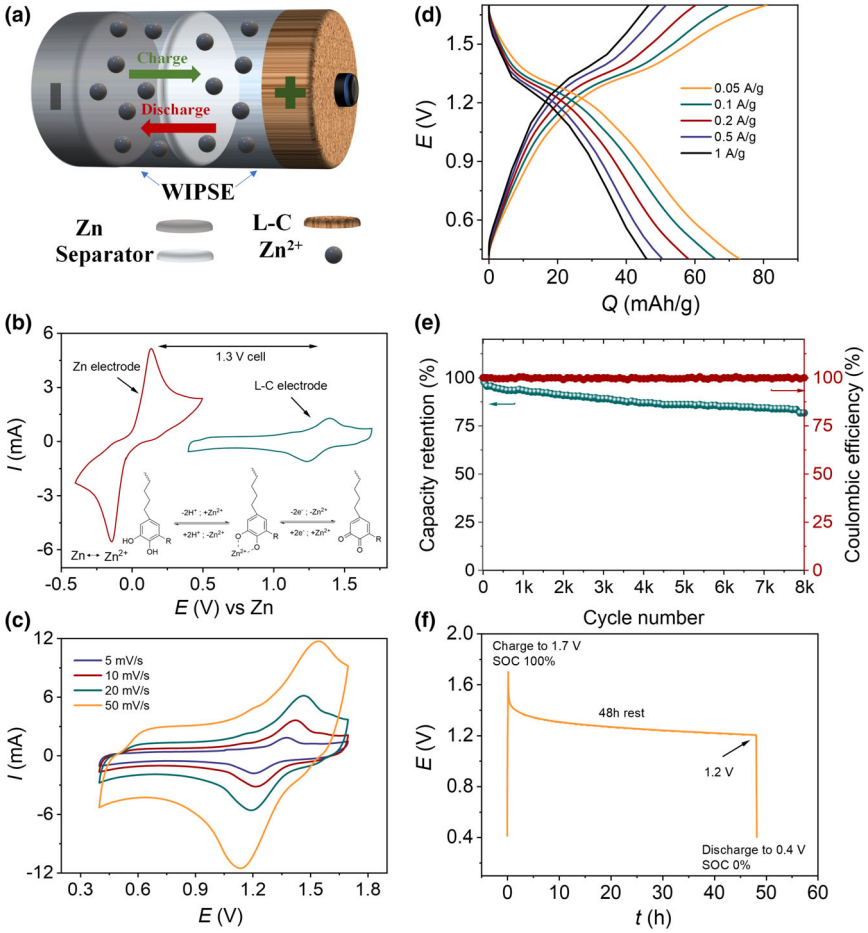

Figure 5. a) Schematic illustration of Zn-lignin battery with WiPSE b) CV of both Zn and L-C electrode in WiPSE showing that the device exhibits 1.3 V of cell potential. c) CV at different sweeps and d) GCD at different current rates of Zn-lignin battery in WiPSE. e) presents capacity retention and coulombic efficiency estimation as cyclic stability analysis of Zn-lignin battery in WiPSE up to 8000 cycles at 1 A g^{-1} current rate. f) Voltage vs time plot for 48 h to analyze the self-discharge of Zn-lignin battery in WiPSE.

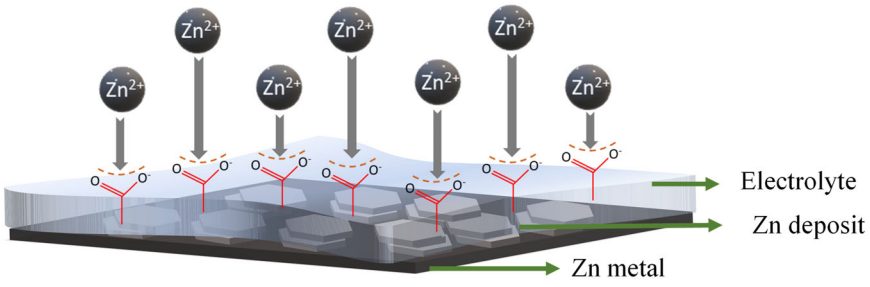

Scheme 1. Schematic of mechanism of uniform Zn deposition in presence of PAA^- polymer on the Zn substrate.

Galvanostatic charge discharge at different current rates were performed to estimate the specific discharge capacity of Zn-lignin cell in hybrid electrolyte (Figure 5d). The discharge curve shows a quasi-plateau within the range from 1.3 to 0.6 V and then the potential drops rapidly at 50 mA g^{-1} of current rate. The device shows a maximum specific capacity of 75 mAh g^{-1} which decreases to 50 mAh g^{-1} (~33% loss in specific capacity) as the current increases about 10 times (500 mA g^{-1} current rate). The fabricated cell displays a maximum of 23 Wh kg^{-1} of specific energy and maximum specific power of 610 W kg^{-1} (Figure S18, Supporting Information). The charge storage process occurs via the migration of Zn^{2+} from the electrolyte and its reduction followed by deposition on Zn during charging step of cell, whereas the deposited Zn is oxidized to Zn^{2+} ions on discharge process. Moreover, the cyclability of the assembled device was tested up to 8000 cycles at 1 A g^{-1} current rate, which retained 80% of its initial capacity with >99% of CE after 8000 cycles (Figure 5e). We also summarize in Table S2, Supporting Information, the performance of various Zn-organic batteries reported in the literature, where except for a few works many suffer to achieve decent cyclic stability. Further, the assembled device underwent a cyclability test of 2000 cycles at low current rates of 0.2 and 0.4 A g^{-1}, demonstrating an impressive 75% capacity retention (Figure S19, Supporting Information). The 80% retention in initial capacity and >99% of CE suggest that this WiPSE electrolyte not only prevents the dissolution of the organic polymer into the electrolyte but also suppresses the side reactions associated with HER, which are both major bottlenecks in the development of organic as well as Zn batteries.

Self-discharge is a challenging issue to avoid in aqueous batteries where one of the electrodes is organic.[37] Also, Zn batteries suffer from self-corrosion and HER in aqueous electrolyte thereby initiating self-discharge in batteries. Therefore, self-discharge of Zn-lignin battery should also be assessed. Herein, the parasitic reactions in Zn-lignin battery were evaluated by monitoring the decay in voltage at open circuit condition for different resting times, i.e., 1, 2, 5, 24, 48, and 72 h. Zn-lignin battery was charged and discharged for 5 cycles at 100 mA g^{-1} in the 1.7–0.4 V voltage range. After the last charging step to 1.7 V, the cell was allowed to rest at OCV for 1 h, then the cell was discharged to 0.4 V. The same protocol was repeated for different OCV rest time 2, 5, 24, 48, and 72 h (Figure S20, Supporting Information). After a 48 h period of rest, the battery exhibits a ~71% and 68% retention of its voltage (indicating a low self-discharge rate of 0.01 V h^{-1}) and specific capacity, respectively, in proposed WiPSE (Figure 5f). Further, the fabricated Zn-lignin battery was subjected to prolonged rest period of 72 h; afterwards, the battery was discharged to 0.4 V at 100 mA g^{-1} current. After 72 h of resting period, the battery retains 63% of its specific capacity supporting our claim of low parasitic side reactions and no dissolution of active material during the rest period.

3. Discussion about Dendrite-Free Zn Deposition

It was observed that utilizing 0.2 m $Zn(TFSI)_2$ in WiPSE exhibited dendrite-free Zn deposition. Based on previous literatures, we propose a hypothesis for uniform, compact, and dendrite-free Zn deposition. The reduction of Zn^{2+} ions on Zn anode is proposed to occur via a "diffusion-controlled" process in the electrolyte, initiated by the migration of Zn^{2+} ions toward the anode under the influence of applied electric field.[38] As these ions reach the anode, uncontrolled 2D diffusion begins leading to lateral diffusion of Zn^{2+} ions to find favorable sites for charge transfer to reduce and plated to form crystal tips. These crystal tips can act as charge centers for further deposition due to the tip effect, potentially forming zinc dendrites. In the presence of electrolytes with functional groups (polyacrylate in this case), it is hypothesized that these electrolytes tend to adsorb onto the Zn electrode surface. Zn^{2+} ions then transferred to the surface through interaction with the functional groups, leading to a uniform electric field distribution.[39–41] This increased nucleation sites may result in uniform Zn deposition. Cross-sectional SEM images (Figure 3c,d) indicate layer-by-layer Zn deposition on Zn anode, suggesting that the presence of PAA^- anions modulates the electric filed, promoting uniform Zn^{2+} diffusion without inducing any concentration difference polarization between regions near the Zn anode and the electrolyte interior.[42] This mechanism explains the creation of densely packed hexagonal Zn crystals, exhibiting no dendritic growth over a 750-cycle duration within a Zn||Zn symmetric device. A schematic representation of Zn growth *via* the (002) plane using the hybrid WiPSE is illustrated in **Scheme 1**. At the metal-electrolyte interface, polyacrylate anions from the electrolyte may adhere to the metal surface, assisting Zn^{2+} ions to reach the interface through the electrostatic potential landscape generated by the negatively charged acrylate groups. However, an analysis of current (i) versus the square root of the scan rate ($\nu^{1/2}$) (depicted in Figure S12b, Supporting Information) during Zn deposition reveals a mass transfer-limited process. This limitation may originate from the orientation of the hydrophobic backbone of polyanions toward the electrode surface, restricting the movement of Zn^{2+} ions and preventing dendritic growth. Under these conditions, Zn growth parallel to the metal surface along the (002) plane is promoted due to constrained diffusion of Zn^{2+} ions. It is important to note that this proposed mechanism is based on previous literature and requires further experimentation to validate this hypothesis.

4. Conclusion

In this work, our objective was to formulate and create a novel hybrid electrolyte functioning as a WiPSE for ZnBs. The primary objective was to leverage a lower concentration of fluorinated salt in creating a WiSE that not only encompasses all the benefits associated with WiSE but also significantly reduces the electrolyte's overall cost. Comparatively, the estimated cost of utilizing PAAK with 0.2 m $Zn(TFSI)_2$ is notably lower

than that of employing higher concentrations of fluorinated salt, such as 1 m $Zn(TFSI)_2$ + 20 m LiTFSI (see Table S3, Supporting Information). Additionally, this study yields compelling evidence that the inclusion of just 0.2 m $Zn(TFSI)_2$ into PAAK yields reversible Zn deposition and dissolution along the (002) plane. After the successful Zn plating/-stripping study in half-cell and solvation structure study, a sustainable Zn-lignin battery was constructed, demonstrating remarkable performance with an outstanding 80% capacity retention after 8000 cycles at a high current rate of 1 A g^{-1}. It achieved a maximum energy output of 23 Wh kg^{-1} and a peak power delivery of 610 W kg^{-1}. This achievement is particularly noteworthy as both lignin and Zn stand as among the most economical, reversible electroactive materials globally. Moreover, they possess the advantages of being non-toxic and readily recyclable. The Zn-lignin battery's appeal lies in the fact that both zinc (at a cost of 0.4 USD Ah^{-1}) and lignin (ranging from 0.1 to 0.4 USD Ah^{-1}) exhibit a favorable low-cost to capacity ratio. This economic advantage positions Zn-lignin batteries as an appealing option in the emerging market of sustainable, large-scale stationary batteries.

5. Experimental Section

5.1. Materials and Chemicals

Softwood kraft lignin was obtained from Bäckhammar. Potassium hydroxide (>85% purity) was purchased from Merck. Zinc bis(trifluoromethanesulfonyl) imide ($Zn(TFSI)_2$) with a purity of 99.5%, potassium acetate (CH_3COOK), and polyacrylic acid (average Mw ≈ 250 000, 35 wt% in H_2O) were all purchased from Sigma Aldrich and used as received. The purchased materials for the project also include conductive carbon (ENSACO 360 G from IMERYS Graphite and Carbon, with a BET surface area of 780 $m^2 g^{-1}$), carboxymethyl cellulose (CMC), and styrene-butadiene rubber (SBR) from TOB New Energy Technology, Xiamen, China, as well as graphite foil (SIGRAFLEX® from SGL Carbon).

5.2. Electrolyte Preparation

Potassium polyacrylate (PAAK) as "water-in-polymer salt electrolyte" was prepared by deprotonating 25 mL polyacrylic acid using aqueous solution of potassium hydroxide until pH become neutral. Thereafter, the obtained solution stirred for 24 h followed by the removal of water by heating this solution at 80 °C. The obtained dry product was dissolved in water in 1:2 wt-ratio (PAAK: water) thereby resulting in the WiPSE.[19] PAAK-$Zn(TFSI)_2$ with 0.1 and 0.2 m concentration was prepared by adding subsequent amount of 0.1 and 0.2 m of $Zn(TFSI)_2$ salt in PAAK (in estimated water content) and stirred at room temperature.[17]

5.3. Lignin-Carbon (L-C) Electrode Preparation

The lignin/carbon (L-C) electrode material was fabricated through solvent-free mechanical milling (ball milling) of conductive carbon and kraft lignin in a planetary ball mill (TOB-XQM-4) using titanium balls. The dry ratio of lignin to carbon was 1:1. Mechanical milling was carried out like the procedure reported previously.[18] The milled powder was then combined with 6 wt% of CMC/SBR (carboxymethyl cellulose/styrene butadiene rubber; 2:4) binder system with water as solvent. The water-based slurry was coated on graphite foil and dried at 60 °C for 1–2 h. The wet thickness was varied between 100 and 400 µm. It was then cut into 16 mm diameter, disk-shaped electrodes for coin cell measurements. The dry weight of the electrodes was between 2 and 4 mg cm^{-2}.

5.4. Electrode and Electrolyte Characterization

Attenuated total reflection Fourier transform infrared spectroscopy (ATR-FTIR) (VERTEX FTIR spectrometer, MA, USA) spectra were recorded for PAAK, and PAAK added different concentration of $Zn(TFSI)_2$ from 400 to 4000 cm^{-1} at 4 cm^{-1} resolution. Rheological studies of the electrolytes were measured using Anton-Paar Rheometer (model MCR 102) at room temperature with a cone plate CP-50-1 using rotational method. Thermogravimetric analysis (TGA) was measured using TA instruments TGA-5500, for the materials thermal stability and plotted rate of weight change as a function of temperature, time. Electrochemical QCM experiments were performed with Au quartz sensors (QSense QSX301) in a QSense Analyzer instrument. In the QCM chamber, the Au quartz sensor served as a working electrode in a 3-electrode setup with a Pt counter and a reference electrode of type WPI Dri-Ref (Ag/AgCl). The electrochemistry was controlled with a Metrohm µAutolab Type III and NOVA 2 software. The frequency changes were transformed into mass changes with the Sauerbrey equation for the third overtone (QSense Dfind software toolbox). Impedance measurements were carried out using an impedance spectrometer (an Alpha high resolution dielectric analyzer, Novocontrol Technologies GmbH) using a two-point probe method. An AC voltage of 5 mV is applied while sweeping the frequency from 105 to 10 Hz, and the measurements were carried out at room temperature. Electrolyte was filled in the Teflon cylindrical cavity of 11.2 mm diameter and length 3.05, and Pt was used as the electrode on either side of the cavity. The final value of the resistance used for the calculation of the ionic conductivity was considered from the linear fitted data. The bulk ionic conductivity was calculated as $\sigma = d/(R \times A)$, where d, A, and R are the distance between the electrodes, area of cross section, and resistance, respectively. Scanning Electron Microscope (SEM) (Zeiss Sigma 500 Gemini) along with the energy dispersive X-ray spectroscopic analysis (EDX) was used to analyze microstructure or morphology of deposited Zn. X-ray diffraction (XRD) measurements were performed for these samples before and after 10 and 100 cycles using a diffractometer (PANalytical X'Pert) with a Cu Kα radiation and a nickel filter in a Bragg–Brentano geometry.

5.5. Cell Fabrication and Electrochemical Characterization

Electrochemical measurements of the full cells were performed by assembling CR2032- type coin cells at ambient condition. The L-C electrodes were used as cathode and had a mass loading of 3.5 mg cm^{-2} whereas Zn was used as anode. A glass fiber type A soaked with PAAK added $Zn(TFSI)_2$ was used as separator. For the device measurement, the cell was charged at different current 0.1–1 A g^{-1} in the potential range of 0.4 and 1.7 V. Galvanostatic Cycling with Potential Limitation (GCPL) technique was used as a testing method for galvanostatic charge discharge (GCD) and sate of charge (SOC) determination. Specific energy (E) and specific power (P) were calculated using the equations below where m is total mass, t is discharging time, i is discharge current, and V is the potential.

$$E = \frac{1}{m}\int_0^t iV dt \tag{2}$$

$$P = \frac{E}{t} \tag{3}$$

Acknowledgment

This work was primarily supported by the Proof-of-Concept project "high-voltage aqueous electrolytes (KAW 2020.0174)" and the "Wood Wallenberg Science Center" funded by Knut and Alice Wallenberg (KAW) foundation. This work is also supported by the Swedish Research Council (2016-05990), the Swedish Government Strategic Research Area in Materials Science on Functional Materials at Linköping University (Faculty Grant SFO-Mat-LiU No. 2009-00971), and the

competence center FunMat-II funded by the Swedish Agency for Innovation Systems (Vinnova, grant no 2016-05156). ZK and RC acknowledge Åforsk foundation for the project "anode free Zn-ion battery (21-130)" and "Zn-lignin battery (22-134)." RC, AM, CMA DK, and ZK acknowledge Swedish Electricity Storage and Balancing Centre (SESBC) funded by Energyimyndiggheten. RS acknowledges support from the Swedish Research Council VR International Postdoc Grant 2022-00213. The authors are grateful to Ligna Energy AB for providing Lignin and scientific discussions. CMA acknowledges "STand UP for energy collaboration and Swedish Research Council (2020-05223)".

Conflict of Interest

The authors declare no conflict of interest.

Supporting Information

Supporting Information is available from the Wiley Online Library or from the author.

Keywords

lignin, sustainable, water-in-salt electrolyte, Zinc, Zn-ion battery

Received: February 22, 2024
Published online: March 9, 2024

[1] Department of Economic and Social Affairs Sustainable Development. United Nations. https://sdgs.un.org/2030agenda. (accessed: September, 2015)
[2] M. Armand, J. M. Tarascon, *Nature* **2008**, *451*, 652.
[3] C. F. Armer, J. S. Yeoh, X. Li, A. Lowe, *J. Power Sources* **2018**, *395*, 414.
[4] L.-F. Zhao, Z. Hu, W.-H. Lai, Y. Tao, J. Peng, Z. C. Miao, Y. X. Wang, S. L. Chou, H. K. Liu, S. X. Dou, *Adv. Energy Mater.* **2021**, *11*, 2002704.
[5] M. Song, H. Tan, D. Chao, H. J. Fan, *Adv. Funct. Mater.* **2018**, *28*, 1802564.
[6] Q. Li, Y. Zhao, F. Mo, D. Wang, Q. Yang, Z. Huang, G. Liang, A. Chen, C. Zhi, *EcoMat* **2020**, *2*, e12035.
[7] M. Iturrondobeitia, O. Akizu-Gardoki, O. Amondarain, R. Minguez, E. Lizundia, *Adv. Sustain. Syst.* **2021**, *6*, 2100308.
[8] F. Wan, J. Zhu, S. Huang, Z. Niu, *Batteries Supercaps* **2020**, *3*, 323.
[9] H. Bi, X. Wang, H. Liu, Y. He, W. Wang, W. Deng, X. Ma, Y. Wang, W. Rao, Y. Chai, H. Ma, R. Li, J. Chen, Y. Wang, M. Xue, *Adv. Mater.* **2020**, *32*, 2000074.
[10] C. Liu, X. Xie, B. Lu, J. Zhou, S. Liang, *ACS Energy Lett.* **2021**, *6*, 1015.
[11] T. Wei, Y. Ren, Y. Wang, L' Mo, Z. Li, H. Zhang, L. Hu, G. Cao, *ACS Nano* **2023**, *17*, 3765.
[12] Z. Khan, D. Kumar, X. Crispin, *Adv. Mater.* **2023**, *35*, e2300369.
[13] L. Suo, O. Borodin, T. Gao, M. Olguin, J. Ho, X. Fan, C. Luo, C. Wang, K. Xu, *Science* **2015**, *350*, 938.
[14] M. Zhang, T. Dong, D. Li, K. Wang, X. Wei, S. Liu, *Energy Fuel* **2021**, *35*, 10860.
[15] Y. Zhao, Y. Wang, Z. Zhao, J. Zhao, T. Xin, N. Wang, J. Liu, *Energy Storage Mater.* **2020**, *28*, 64.
[16] F. Wang, O. Borodin, T. Gao, X. Fan, W. Sun, F. Han, A. Faraone, J. A. Dura, K. Xu, C. Wang, *Nat. Mater.* **2018**, *17*, 543.
[17] D. Kumar, U. Ail, Z. Wu, E. M. Björk, M. Berggren, V. Gueskine, X. Crispin, Z. Khan, *Adv. Sustain. Syst.* **2023**, *7*, 2200433.
[18] U. Ail, J. Phopase, J. Nilsson, Z. U. Khan, O. Inganäs, M. Berggren, X. Crispin, *ACS Sustain. Chem. Eng.* **2020**, *8*, 17933.
[19] Z. Khan, U. Ail, F. Nadia Ajjan, J. Phopase, Z. Ullah Khan, N. Kim, J. Nilsson, O. Inganäs, M. Berggren, X. Crispin, *Adv. Energy Sustain. Res.* **2022**, *3*, 2100165.
[20] Z. Khan, A. Martinelli, L. R. Franco, D. Kumar, A. Idström, L. Evenäs, C. M. Araujo, X. Crispin, *Chem. Mater.* **2023**, *35*, 6382.
[21] P. Li, B. P. Roberts, D. K. Chakravorty, K. M. Merz Jr., *J. Chem. Theory Comput.* **2013**, *9*, 2733.
[22] E. M. Morais, A. Idström, L. Evenäs, A. Martinelli, *Molecules* **2023**, *28*, 5147.
[23] S. P. Gejji, K. Hermansson, J. Lindgren, *J. Phys. Chem.* **1993**, *97*, 3712.
[24] Y. Umebayashi, T. Yamaguchi, S. Fukuda, T. Mitsugi, M. Takeuchi, K. Fujii, S. I. Ishiguro, *Anal. Sci.* **2008**, *24*, 1297.
[25] C. Zhang, J. Holoubek, X. Wu, A. Daniyar, L. Zhu, C. Chen, D. P. Leonard, I. A. Rodríguez-Pérez, J. X. Jiang, C. Fang, X. Ji, *Chem. Commun.* **2018**, *54*, 14097.
[26] Y. Wang, Y. Lei, C. Zhou, B. Wu, Y. Jiang, J. Lei, *Eur. Polym. J.* **2019**, *118*, 474.
[27] C. Lin, X. Zhang, X. Qiang, J.-S. Zhang, Z.-J. Tan, *J. Chem. Phys.* **2019**, *151*, 114902.
[28] H. G. de Jong, J. Lyklema, H. P. van Leeuwen, *Biophys. Chem.* **1987**, *27*, 173.
[29] M. Plata, S. Olvera, C. Ramírez-Rodríguez, H. Dorantes-Rosales, E. M. Arce-Estrada, *ECS Trans.* **2007**, *3*, 25.
[30] A. V. Kosov, O. V. Grishenkova, O. L. Semerikova, V. A. Isaev, Y. P. Zaikov, *J. Electroanal. Chem.* **2021**, *883*, 115056.
[31] D. E. Ciurduc, C. D. L. Cruz, N. Patil, A. Mavrandonakis, R. Marcilla, *Energy Storage Mater.* **2022**, *53*, 532.
[32] J. Zheng, Q. Zhao, T. Tang, J. Yin, C. D. Quilty, G. D. Renderos, X. Liu, Y. Deng, L. Wang, D. C. Bock, C. Jaye, D. Zhang, E. S. Takeuchi, K. J. Takeuchi, A. C. Marschilok, L. A. Archer, *Science* **2019**, *366*, 645.
[33] M. Zhou, S. Guo, J. Li, X. Luo, Z. Liu, T. Zhang, X. Cao, M. Long, B. Lu, A. Pan, G. Fang, J. Zhou, S. Liang, *Adv. Mater.* **2021**, *33*, e2100187.
[34] J. Cao, D. Zhang, C. Gu, X. Wang, S. Wang, X. Zhang, J. Qin, Z. S. Wu, *Adv. Energy Mater.* **2021**, *11*, 2101299.
[35] Y. Hao, D. Feng, L. Hou, T. Li, Y. Jiao, P. Wu, *Adv. Sci. (Weinh).* **2022**, *9*, e2104832.
[36] M. Egashira, *Electrochemistry* **2022**, *90*, 57001.
[37] D. Kumar, Z. Khan, U. Ail, J. Phopase, M. Berggren, V. Gueskine, X. Crispin, *Adv. Energy Sustain. Res.* **2022**, *3*, 2200073.
[38] W. Lu, C. Xie, H. Zhang, X. Li, *ChemSusChem* **2018**, *11*, 3996.
[39] Q. Zhang, J. Luan, L. Fu, S. Wu, Y. Tang, X. Ji, H. Wang, *Angew. Chem. Int. Ed.* **2019**, *58*, 15841.
[40] H. Li, Z. Liu, G. Liang, Y. Huang, Y. Huang, M. Zhu, Z. Pei, Q. Xue, Z. Tang, Y. Wang, B. Li, C. Zhi, *ACS Nano* **2018**, *12*, 3140.
[41] M. Qiu, P. Sun, Y. Wang, L. Ma, C. Zhi, W. Mai, *Angew. Chem. Int. Ed.* **2022**, *61*, e202210979.
[42] Y. Liang, M. Qiu, P. Sun, W. Mai, *Adv. Funct. Mater.* **2023**, *33*, 2304878.